applied optics

# Dynamic microscopic 3D shape measurement based on marker-embedded Fourier transform profilometry

Yan Hu,[1,2,5] Qian Chen,[1,4] Yuzhen Zhang,[1,3] Shijie Feng,[1,2] Tianyang Tao,[1,2] Hui Li,[1,2] Wei Yin,[1,2] and Chao Zuo[1,2,*]

[1]Jiangsu Key Laboratory of Spectral Imaging & Intelligent Sense, Nanjing University of Science and Technology, Nanjing, Jiangsu Province 210094, China
[2]Smart Computational Imaging (SCI) Laboratory, Nanjing University of Science and Technology, Nanjing, Jiangsu Province 210094, China
[3]Ministerial Key Laboratory of JGMT, Nanjing University of Science and Technology, Nanjing, Jiangsu Province 210094, China
[4]e-mail: chenqian@njust.edu.cn
[5]e-mail: huyanjackson@163.com
*Corresponding author: surpasszuo@163.com

Received 23 June 2017; revised 26 December 2017; accepted 26 December 2017; posted 2 January 2018 (Doc. ID 300792); published 29 January 2018

**In recent years, the fringe projection profilometry (FPP) technique has shown great prospects in the field of dynamic 3D measurement of microscopic surface shape. However, under dynamic conditions, it is desirable to use fewer projected patterns to minimize the sensitivity to motion. The commonly used phase-shifting method needs at least three fringe patterns to retrieve the wrapped phase, which depends heavily on the high-speed hardware to alleviate the effect of motion. Besides, to achieve an unambiguous measurement, at least two wrapped phase maps are required to obtain the absolute phase map, resulting in six pattern projections. In this paper, we propose the marker-embedded Fourier transform profilometry (MEFTP), which extends the modified Fourier transform profilometry with two embedded markers suited to assist the phase-unwrapping process. Combining the embedded markers with temporal phase difference information, the absolute phase can be reliably reconstructed with only two projected patterns. Furthermore, since the phase information is only encoded within a single high-frequency fringe, MEFTP is more suitable for measuring fast-moving or surface-changing objects compared with the phase-shifting method. Experiments on both static and dynamic scenes are performed, verifying that our method can achieve an accurate and robust measurement of a vibrating diaphragm at the speed of 200 frames per second.** 

***OCIS codes:*** (120.5050) Phase measurement; (150.6910) Three-dimensional sensing; (330.1400) Vision - binocular and stereopsis.

https://doi.org/10.1364/AO.57.000772

## 1. INTRODUCTION

In recent years, mechanical testing of materials and structures in micro-electro-mechanical system (MEMS) plays an important role towards the achievement of optimal designs. In the meantime, dynamic profilometry is of great importance when analyzing the behavior of micro-scale products, like the motion-versus-drive signal and shape changes during actuation. As a classic 3D shape measurement technique, fringe projection profilometry (FPP) has been widely used in surface profiling of macro-scale objects for its advantages of flexibility, non-contactness, and high accuracy [1]. Recent progress in high-speed-camera and digital-projection technology is currently enabling the use of FPP under time-critical, e.g. dynamic, real-time conditions [2–6]. On the other hand, high-speed, real-time measurement of the 3D topography of the microscopic specimen is also becoming increasingly important in various fields, such as online inspection and quality control. In our recent work, a stereomicroscope arrangement is extended to 3D micro-profilometer based on the fringe projection technique [7]. By using a digital micromirror device (DMD)-based digital projector as the fringe-generating element, it is convenient to generate customized structured fringe patterns for 3D shape reconstruction.

When applying FPP in the measurement of dynamic scenes, it is necessary to reduce the measurement time as well as image-acquisition number to minimize the motion-induced measurement error. The commonly used phase-shifting method needs at least three phase-shifted sinusoidal fringe patterns to retrieve

the wrapped phase, which represents the originally projected phase *modulo* $2\pi$. The inherent phase ambiguity further requires temporal phase unwrapping using a large number of additional patterns [8,9], which greatly limits the application of phase shifting in time-critical conditions. In order to achieve high-speed measurement and reduce the effect of motion, high-speed hardware, like digital light processing (DLP) projectors and high-speed cameras, are usually required. By combining the binary projection techniques with lens defocusing [10,11], the fringe projection speed can be increased to kilohertz (kHz) or even tens of kHz [12].

Compared with the phase-shifting method, Fourier transform profilometry (FTP) can retrieve 3D information using only one or two images [2,13,14], which is more suitable for dynamic measurement. Nevertheless, the absolute or unwrapped phase value cannot be directly obtained through phase-shifting FPP or FTP because the phase value derived from both methods is wrapped in $[-\pi, \pi)$. To acquire the continuous phase map from a wrapped phase map, spatial phase-unwrapping methods can be applied without requiring additional information [15–17]. However, since these methods are based on only the phase information of spatial neighboring pixels with no reference phase value, they cannot determine the period numbers and the absolute phase range correctly and unambiguously. In other words, it can only yield a continuous (but not "absolute") phase that is relative to one point, which is usually the starting point of the phase-unwrapping algorithm with its absolute phase value remaining undetermined. In order to determine the absolute phase without projecting an additional pattern, one can embed an easily distinguishable marker with known absolute phase value into the pre-coded fringe pattern [18,19]. Once the marker is detected, the absolute phase can be obtained by shifting the whole phase map with respect to the marker point phase. However, the correct detection rate of the marker is strongly sensitive to the intensity change of the image caused by various degradations during image capture, e.g., deformation, resampling, attenuation, defocus, and surface reflectivity variations. A misjudgment or erroneous judgment of marker position will lead to a total failure in phase unwrapping, resulting in an erroneous and unstable 3D reconstruction.

In this paper, we propose the marker-embedded Fourier transform profilometry (MEFTP), which extends the modified FTP with two embedded markers suited to assist the phase-unwrapping process and improve the robustness of absolute phase retrieval. The two markers are designed in a cross shape but with opposite intensity distributions. They are complementary in the two patterns and can be effectively canceled during the phase calculation. In the absolute phase recovering process, the detected positions of the two markers are used to determine the fringe orders. When the detected two markers provide the same fringe orders that need to be compensated for, the phase unwrapping is considered reliable. However, when the derived fringe orders are different, we introduce temporal phase difference information to help confirm the fringe orders, which is based on the reasonable assumption that the phase values between two consecutive frames only vary in a very small range. By combining the two embedded markers with temporal phase difference information, the absolute phase can be reliably reconstructed with only two projected patterns. In the experiments, the measurement uncertainty in depth is verified by measuring a ceramics plate, which has a root-mean-square error (RMSE) value of 3.4 μm. The dynamic 3D measurements of a vibrating diaphragm using phase-shifting FPP and MEFTP are also presented, verifying that our method is much less sensitive to motion compared with the phase-shifting method.

## 2. MODIFIED FTP

FTP was first introduced by Takeda *et al.* for fringe-pattern analysis [20]. In FTP, usually a high-frequency fringe pattern is projected onto the object surface, and the fringe pattern designed in the projector space can be expressed as

$$I_p(x_p, y_p) = a_p + b_p \cos(2\pi f_p x_p), \tag{1}$$

where $a_p$ is the average value, $b_p$ is the amplitude, $(x_p, y_p)$ is the projector's coordinate, and $f_p$ is the frequency of the sinusoidal fringe. Without loss of generality, here we assume that the fringes are oriented perpendicular to the $x_p$ axis, which will be used when triangulating with the camera. The pattern is sent to the projector and then projected onto the object. The projected fringe pattern combined with the ambient light is modulated and reflected by the object. The captured image in FTP then can be expressed as

$$I_c(x_c, y_c) = a_c(x_c, y_c) + b_c(x_c, y_c) \cos[\Phi(x_c, y_c)], \tag{2}$$

where $(x_c, y_c)$ is the pixel coordinate of the camera, and $a_c$ and $b_c$ are the background intensity and the modulation of the fringe, respectively. $\Phi(x_c, y_c) = 2\pi(f_0 x_c) + \phi(x_c, y_c)$. $f_0$ is the carrier frequency of the captured fringe image, and $\phi$ is the modulated phase, which is the key factor containing the 3D information of measured objects. Using Euler's formula, we can simplify Eq. (2) as the following exponential form:

$$I_c = a_c + \frac{b_c}{2}[\exp(i\Phi) + \exp(-i\Phi)]. \tag{3}$$

The 2D Fourier transform of Eq. (3) is

$$G(f_x, f_y) = A(f_x, f_y) + B(f_x, f_y) + B^*(-f_x, -f_y), \tag{4}$$

where $G(f_x, f_y)$, $A(f_x, f_y)$, and $B(f_x, f_y)$ are the Fourier transforms of $I_c$, $a_c$, and $(b_c/2)\exp(i\Phi)$, respectively. $B^*(f_x, f_y)$ is the complex conjugate of $B(f_x, f_y)$. The Fourier shift theorem indicates that multiplying a carrier phase factor in spatial domain is equivalent to a translation of the signal spectrum in the frequency domain, so the three terms are separated to certain extent in the Fourier domain, as shown in Figs. 1(a) and 1(b).

In conventional FTP, $a_c$, $b_c$, and $\phi$ are assumed to vary slowly compared with the carrier frequency so that a band-pass filter can be applied to extract the primary order of spectrum part $B(f_x, f_y)$. However, conventional FTP has its limitation when measuring complex objects because the primary spectral component $B(f_x, f_y)$ in Eq. (4) may be overlapped by the zero-frequency term $A(f_x, f_y)$, as shown in Fig. 1(b), especially when the fringe's carrier frequency is not high enough. To alleviate the spectrum overlapping problem, the $\pi$-shift FTP method was proposed [21,22] to effectively suppress the zero order by projecting an additional $\pi$-shift sinusoidal fringe image,

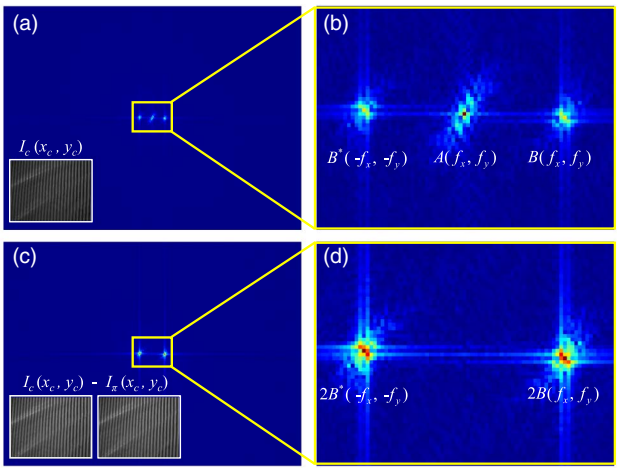


**Fig. 1.** Spectrum comparison of conventional FTP and $\pi$-shift FTP. (a) Spectrum of a raw fringe image from conventional FTP; (b) magnified spectrum of the central part in (a); (c) spectrum after subtracting the $\pi$ shift image from the original image; (d) magnified spectrum of the central part in (c).

$$I_\pi(x_c, y_c) = a_c(x_c, y_c) + b_c(x_c, y_c)\cos[\Phi(x_c, y_c) + \pi]. \quad (5)$$

By taking the difference between $I_c(x_c, y_c)$ and $I_\pi(x_c, y_c)$, the fundamental frequency information is doubled with the zero-frequency term being effectively canceled,

$$I_d = I_c - I_\pi = b_c[\exp(i\Phi) + \exp(-i\Phi)]. \quad (6)$$

The 2D spectrum of $I_d$ is as shown in Fig. 1(c), which only contains the $\pm 1$ orders of the primary spectrum parts. In this form, the wanted primary orders of the spectrum part can be much easier to be filtered out by a band-pass filter. Applying the inverse Fourier transform to the extracted $2B(f_x, f_y)$, we can obtain the complex field with the phase component $\Phi$ included as

$$I_{\text{inv}} = b_c \exp(i\Phi). \quad (7)$$

Note that the quality of the derived fringe represented by Eq. (7) can be further improved using denoising algorithms such as windowed Fourier transform (WFT) [23]. The wrapped phase corresponding to $\Phi$ can be extracted by

$$\Phi_w = \arctan\frac{\text{Im}(I_{\text{inv}})}{\text{Re}(I_{\text{inv}})}. \quad (8)$$

However, the $\pi$-shift method is very sensitive to motion because the phase information is encoded in two sinusoidal fringes and thus the ripples will be inevitably introduced into the 3D result when measuring a dynamic scene. To address this problem, modified FTP [18] was developed by projecting another pattern with uniform intensity distribution ($I_0(x_p, y_p) = a_p$) instead of the $\pi$-shift fringe pattern. The corresponding captured intensity of this pattern directly gives the background intensity

$$I_0(x_c, y_c) = a_c(x_c, y_c). \quad (9)$$

By taking the difference between $I_c$ and $I_0$, the zero-frequency term can also be effectively removed,

$$I'_d = I_c - I_0 = \frac{b_c}{2}[\exp(i\Phi) + \exp(-i\Phi)]. \quad (10)$$

In this form, the wrapped phase $\Phi_w$ can also be obtained using Eq. (8) after getting the inverse Fourier transform of the primary spectrum. By using modified FTP, the sensitivity to motion is much smaller compared with $\pi$-shift FTP because only one fringe image contains phase information. However, FTP methods cannot provide an absolute phase map that is used to derive quantitative height information. In our proposed technique, we extend the modified FTP by embedding specially designed markers to assist the absolute phase-unwrapping process. This will be detailed in the next section.

## 3. ABSOLUTE PHASE RETRIEVAL BASED ON MEFTP

When using the FTP-based algorithms described in Section 2 for phase measurement, the acquired phase map is wrapped within its principal values ranging between $-\pi$ and $\pi$, which means the fringe order information is lost. In order to recover the fringe orders and obtain the absolute phase map of the surface, a phase-unwrapping process has to be performed. In general, for smooth and continuous surfaces, the $2\pi$ phase wraps can be removed by using a spatial phase-unwrapping algorithm. However, the conventional spatial phase-unwrapping algorithm, for example, the quality-guided phase unwrapping [15], starts from the highest-fringe-quality pixel and uses it as the phase reference point, then goes on to the lower quality ones following a path guided by the fringe quality. However, since the fringe order of this starting point (or reference point) is still unknown, there is no guarantee that the spatially unwrapped phase map $\Phi'$ could coincide with the absolute phase map $\Phi$. As the absolute phase map is directly related to depth information and used during the calibration stage, we have to compensate for the difference between the spatially unwrapped phase $\Phi'$ and the true absolute phase $\Phi$ in order to retrieve the depth information correctly by

$$\Phi = \Phi' + n \times 2\pi. \quad (11)$$

Here, $n$ is the unknown fringe order number that should be further compensated. Researchers have come up with ideas that embed a marker in the fringe pattern to adjust the relative fringe order $n$ to be absolute [18,24–26]. For example, Guo and Huang [18] proposed to use a fringe pattern $I'_p(x_p, y_p)$ and a flat pattern $I'_0(x_p, y_p)$ with a cross-shaped marker embedded as shown in Fig. 2(b). The central coordinate of the cross marker corresponds to a fixed absolute phase value $\Phi_m$. The corresponding pixels in the fringe pattern

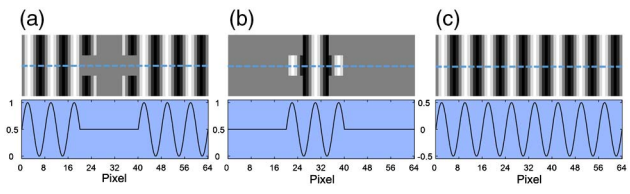


**Fig. 2.** Fringe patterns of one embedded marker. (a) Embedded marker in the fringe pattern; (b) embedded marker in the flat pattern; (c) the difference between the fringe pattern and the flat pattern.

$I'_p(x_p, y_p)$ are replaced by constant intensity as shown in Fig. 2(a). When subtracting Fig. 2(b) from Fig. 2(a), the result only contains the sinusoidal component as shown in Fig. 2(c).

The marker-embedded patterns $I'_p(x_P, y_P)$ and $I'_0(x_P, y_P)$ are projected in sequence, and the corresponding fringe image and flat image are captured. Then the marker is detected in the flat image by using template matching with the same intensity distribution as the marker. The phase value at the marker's center is extracted as $\Phi'_m$ after getting the unwrapping phase map. At last, the relative fringe order $n$ is obtained by

$$n = \text{round}(\Phi_m - \Phi'_m)/2\pi, \tag{12}$$

where round is the nearest integer returned function. This marker-embedded method facilitates the retrieval of the absolute phase map from only two images based on FTP analysis, which improves the measurement accuracy while preserving its potential measurement speed.

Working under most conditions, this method could encounter problems when measuring dynamic scenes because the projected marker may shift to an irregular area and be distorted heavily, as illustrated in Fig. 3. In this case, there is a serious risk that the marker cannot be correctly detected, which will destroy the whole 3D reconstruction. To solve this problem, we propose the MEFTP technique to compensate for the phase difference by embedding two specially designed markers instead of only one. The second marker is designed to have a total opposite intensity distribution compared to the first one, making both of these two markers easily distinguishable and detectable, as is shown in Fig. 4(b). Similarly, by subtracting Fig. 4(b) from Fig. 4(a), the marker can also be canceled as shown in Fig. 4(c). The two markers are preset at two locations in the projector space, denoting two predefined absolute phase values $\Phi_{m_1}$ and $\Phi_{m_2}$. A marker removal example measuring an earphone diaphragm is shown in Fig. 5. After subtracting Fig. 5(b) from Fig. 5(a), both the background bias and the markers are removed without changing the fringe information, which can be seen in Fig. 5(c).

Even though the two-marker scheme can provide a double proofed relative fringe order, there is still a limited chance that the two markers give contradictory estimates. To further secure the fringe order compensation process, we also exploit the phase difference information along the temporal axis. For high-speed imaging conditions, the time interval between the consecutive frames is usually small so that the phase difference between two adjacent measurements is typically less than $\pi$. This assumption is utilized to further confirm the fringe order only when the two markers give inconsistent relative fringe order estimates. The flowchart of the whole method is shown in Fig. 6. First, the

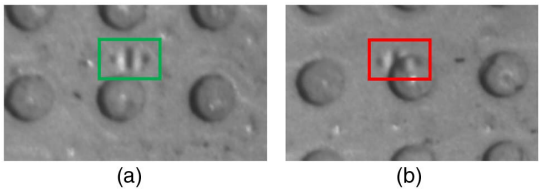


**Fig. 3.** Illustration of marker shift to an irregular area. (a) Example of a detectable marker in a regular area; (b) example of a deformed marker in an irregular area.

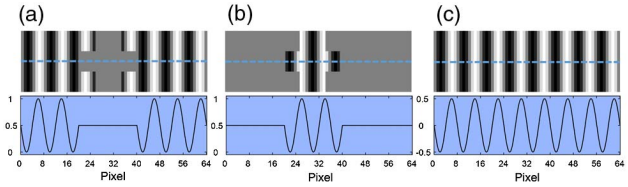


**Fig. 4.** Fringe patterns of the other embedded marker. (a) Embedded marker in the fringe pattern; (b) embedded marker in the flat pattern; (c) the difference between the fringe pattern and the flat pattern.

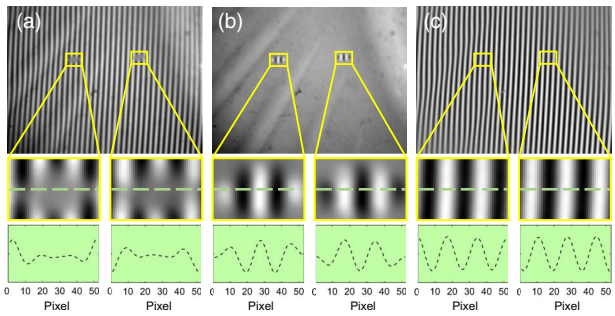


**Fig. 5.** Marker removal example measuring an earphone diaphragm. (a) Marker-embedded fringe pattern and the magnified marker details; (b) marker-embedded flat image and the magnified marker details; (c) the fringe after subtraction and the magnified marker details.

wrapped phase $\Phi_w$ is calculated using Eq. (8), and then the quality-guided phase-unwrapping algorithm is applied to get the initial continuous phase map $\Phi'$. The phase values of the extracted markers' positions are noted as $\Phi'_{m_1}$ and $\Phi'_{m_2}$, respectively. The absolute phase map $\Phi$ can be obtained by adding $n \times 2\pi$ to $\Phi'$, where $n$ is derived by comparing $(\Phi'_{m_1}, \Phi'_{m_2})$ and $(\Phi_{m_1}, \Phi_{m_2})$. Specifically, the comparison starts with getting

$$n_1 = \text{round}[(\Phi_{m_1} - \Phi'_{m_1})/2\pi], \tag{13}$$

$$n_2 = \text{round}[(\Phi_{m_2} - \Phi'_{m_2})/2\pi]. \tag{14}$$

If $n_1 = n_2$, it means both the two markers are correctly detected, and thus $n = n_1$ (or $n_2$). We then get $\Phi$ by Eq. (11) as represented by the green line in Fig. 6. However, in case that $n_1 \neq n_2$, which means the derived fringe orders from the two markers are different, we introduce the temporal phase difference information to help conform the fringe orders. Because the frame rate of the camera is very high, the time interval between two captured frames is small, so the phase difference of each pixel at two neighboring moments would be less than $\pi$ based on the reasonable assumption that the captured images do not change dramatically. Assume $\Phi_l$ is the last derived true absolute phase map of the scene, so we can use the relation $\Phi \in [\Phi_l - \pi, \Phi_l + \pi)$. Then we can get

$$n' = \text{round}[\text{average}(\Phi_l - \Phi')/2\pi] \tag{15}$$

as a reference to figure out which maker is correctly detected. If $n' = n_1$ (or $n_2$), which means one of the markers is correctly

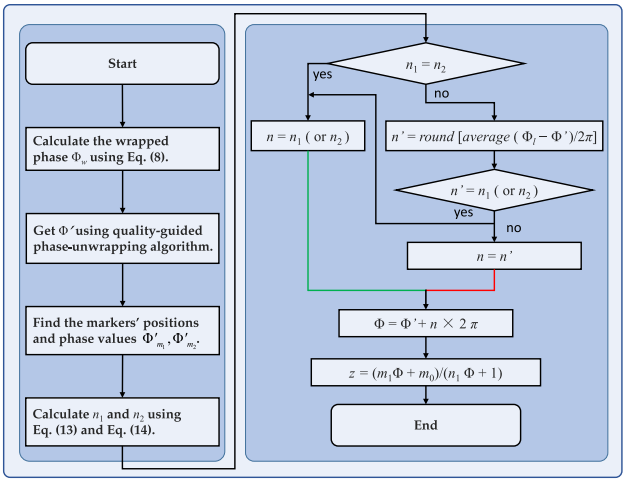


**Fig. 6.** Flowchart of the absolute phase retrieval process based on the embedded markers.

detected, we can also get $\Phi$ by Eq. (11) as represented by the green line in Fig. 6. However, if $n' \neq n_1$ (and $n_2$), this means none of the markers are incorrectly detected. In this case, we use $n'$ directly to get $\Phi$, following the red line in Fig. 6. It should be noted that because the spatial phase unwrapping can only cope with smooth phase distribution defined in a simply connected region, our method may fail in cases when the measured scene contains discontinuous surfaces or multiple isolated objects.

## 4. PHASE–HEIGHT CONVERSION

The FPP-based 3D shape measurement technique is concerned with extracting the geometry information from the images of the measured object. The basic principle is optical triangulation. The system consists of a camera and a projector arranged in a triangulation configuration based on a stereo microscope. The camera captures the fringe images, which are modulated by the shape of the measured object. After getting the absolute phase map $\Phi$ using the proposed MEFTP method, we are able to convert the absolute phase map $\Phi$ into the depth information base on the calibrated relation between phase and height. In this section, we discuss the phase-to-height mapping algorithm, which converts the absolute phase map of the object into a dense 3D point cloud representing the object's surface.

In order to calibrate the relation between phase and height, we should make sure that the absolute phase map using MEFTP has the same definition as the phase map defined in the calibration stage, which means the system should also be calibrated using absolute phase maps. To clearly clarify the calibration procedure, we begin with the basic optical system of our setup, which is illustrated in Fig. 7(a). A stereomicroscope is used as the basic instrument, which is composed of two totally separate coaxial optical paths. The projector is fixed upon the left optical path and the camera is fixed on an adapter, which shares the other optical path by a beam splitter. The two light paths of the stereomicroscope, combined with the camera and the projector, constitute a triangular structure. The projector's optical path contains not only the projector lens but also the lenses inside one beam path of the stereomicroscope; thus the traditional calibration method established by several general parameters is no longer applicable [27]. Even so, for each camera pixel $(x_c, y_c)$, we still can establish a geometric relation between the absolute phase value $\Phi(x_c, y_c)$ and the depth information $z(x_c, y_c)$ based on the triangulation relation introduced above.

The geometric relation can be derived according to the coordinate system of the system as shown in Fig. 7(b). $O - XYZ$ denotes the world coordinate system. $O_C - X_C Y_C Z_C$ is the camera coordinate system, and $O_P - X_P Y_P Z_P$ is the projector coordinate system. $o_c - x_c y_c$ is defined in the camera space, and $o_p - x_p y_p$ is defined in the projector space. $O_C O'_C$ and $O_P O'_P$ are the optical axes of the camera and the projector, respectively. $H$ and $H'$ mean the principal points of the microscope part in the projector's light path, which includes the eyepiece, the tube lenses, the zoom lenses, and the objective. For each pixel of

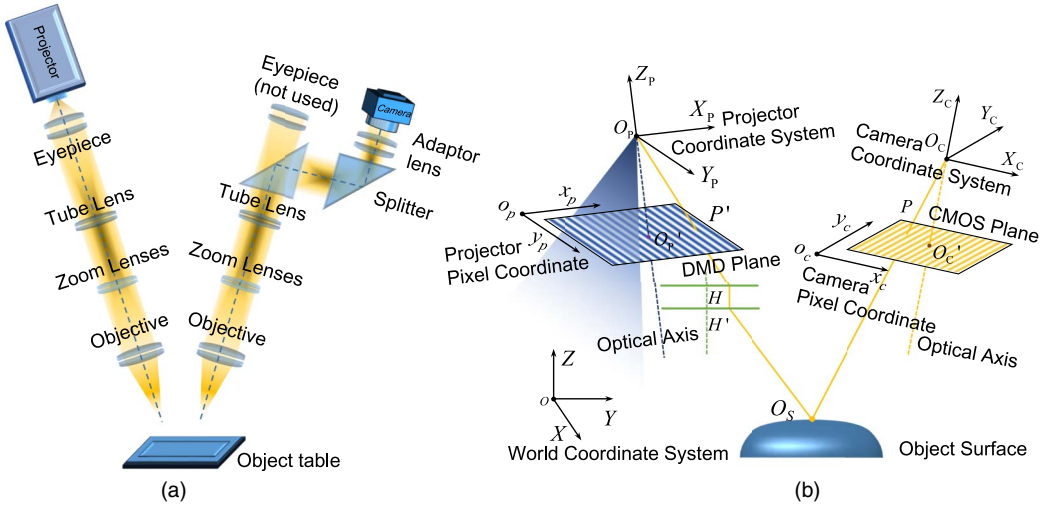


**Fig. 7.** Light path construction and the geometric relationship of the setup. (a) The basic light path in our system setup; (b) the coordinate systems in our system setup.

the camera, there exists a virtual line passing through its projection center $O_C$ and the pixel itself. For example, pixel $P$ on the CMOS plane corresponds to a principal ray $O_CP$, which is reflected from point $O_S$ on the object surface and then passes through $O_C$. Inversely tracing this ray into the other optical path, it first passes through $HH'$, then the projection center $O_P$ of the projector, and finally intersects the DMD plane at point $P'$. The absolute phase value calculated at pixel $P$ based on the captured images should be the same as the absolute phase value predefined at $P'$ in the projector space. According to our previous work [28], the relation between the depth $z$ in the world coordinate and the absolute phase $\Phi$ is modeled as

$$z(x_c, y_c) = \frac{m_1(x_c, y_c)\Phi(x_c, y_c) + m_0(x_c, y_c)}{n_1(x_c, y_c)\Phi(x_c, y_c) + 1}, \quad (16)$$

where $m_0$, $m_1$, and $n_1$ are constant coefficients, and note that each camera pixel $(x_c, y_c)$ has its own corresponding set of $(m_0, m_1, n_1)$. The phase–height relation is described in a nonlinear expression, which is actually determined by the nontelecentric character of the projector's light path. A smaller $n_1$ indicates a more linear relation and larger depth of field.

In order to calibrate the coefficients in Eq. (16), we need at least three pairs of $(z, \Phi)$ for polynomial curve fitting. The calibration procedure of the phase-to-height relation is illustrated in Fig. 8 (where $m$ is the number of equidistant positions in the $z$ direction). A flat board is used here as a reference plane. When the board is moved to a preset position $z$, the multifrequency phase-shifting method [9] is applied to calculate the absolute phase $\Phi$, and then a pair of $(z, \Phi)$ is obtained. In this paper, we use 20 equally separated planes distributed within a calibrated range of 4 mm in the $z$ direction, which almost covers the whole depth of the field of the stereomicroscope. After getting 20 pairs of $(z, \Phi)$, we can establish an overdetermined set of equations with three unknowns for each camera pixel as

$$\begin{bmatrix} \Phi_1 & -z_1\Phi_1 & 1 \\ \vdots & \vdots & \vdots \\ \Phi_m & -z_m\Phi_m & 1 \end{bmatrix} \begin{bmatrix} m_1 \\ n_1 \\ m_0 \end{bmatrix} = \begin{bmatrix} z_1 \\ \vdots \\ z_m \end{bmatrix}, \quad m = 20, \quad (17)$$

which can be easily solved using the least-squares algorithm. When all coefficients in Eq. (16) are determined, we can use it to convert the absolute phase measurement $\Phi$ into the depth information of the measured object.

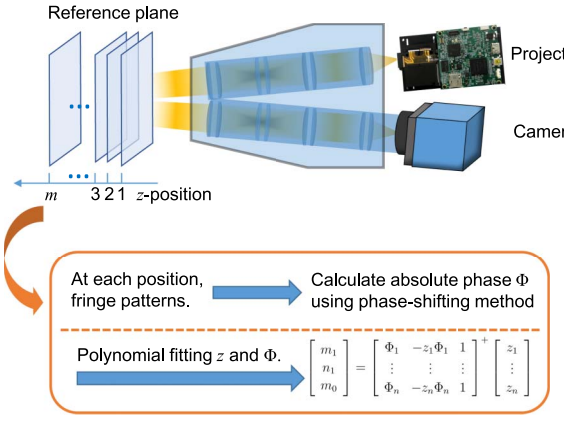


**Fig. 8.** Calibration procedure of the phase-to-height relation.

## 5. EXPERIMENTS

Based on the system depicted in Fig. 7, we applied the proposed MEFTP technique in 3D shape measurement of both static and dynamic scenes. First, the measurement uncertainty in depth using conventional FTP and MEFTP is compared by measuring a ceramic plate. Figures 9(a) and 9(b) are the 2D spectrums of the fringe images using conventional FTP and MEFTP, respectively. Because of the elimination of the zero-frequency term, the ±1 order of the spectrum parts using MEFTP is totally separated compared with that using conventional FTP. By the inverse 2D Fourier transform of the primary order of the spectrums, as marked by the red rectangle in Figs. 9(a) and 9(b), we obtain the complex field $I_{inv}$ corresponding to both methods. Then the height distribution $z$ can be calculated using Eq. (16) after getting the absolute phase map. By using the MEFTP method, the spectrum aliasing effect is effectively alleviated, which considerably benefits the improvement of measurement accuracy. Figures 9(c) and 9(d) are the error distributions reconstructed from Figs. 9(a) and 9(b), respectively. The RMSE of the measurement results is 8.8 μm and 3.4 μm, respectively. MEFTP improves the accuracy more than two times compared with the conventional FTP.

In order to test the effectiveness in detail resolving, we measured two sub-areas of a printed circuit board (PCB). Figures 10(a) and 10(b) show the measured areas marked in red rectangles, which contain both etched pins with solder-resist ink around them and microstrip lines covered with solder-resist ink. The thickness of the etched metal on the

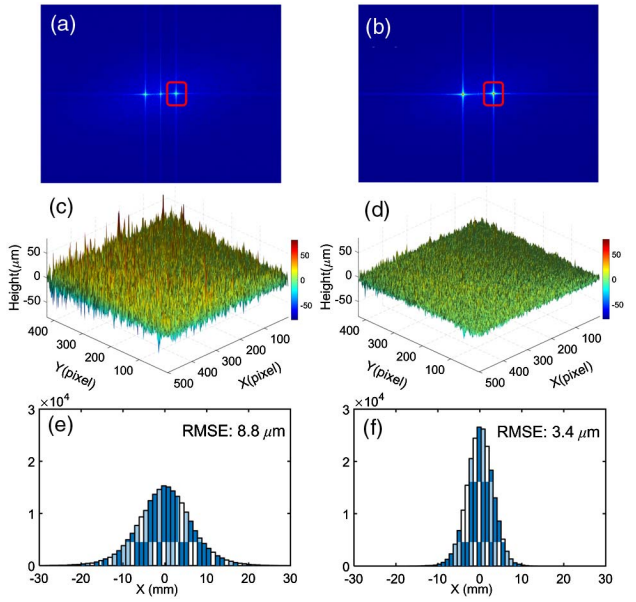


**Fig. 9.** Measurement uncertainty comparison using conventional FTP and MEFTP. (a) and (b) are the spectrums of fringe by using conventional FTP and proposed FTP methods, respectively; (c) and (d) are the error distribution reconstructed from (a) and (b), respectively; (e) and (f) are the root-mean-square error (RMSE) of the measurement results.

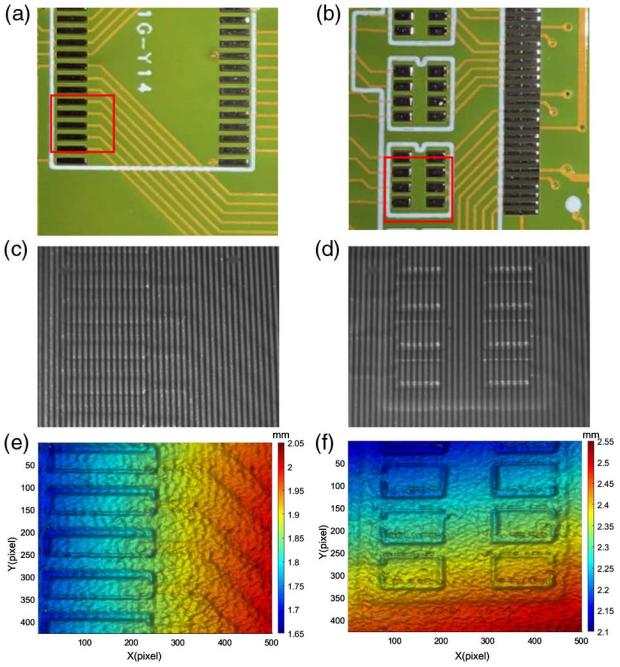


**Fig. 10.** Measurement result of the structures on a PCB. (a) and (b) show the measured areas of interest marked in red rectangles; (c) and (d) are the measured areas containing both metal pads with the solder-resist oil around them and some wires covered with solder-resist oil; (e) and (f) are the retrieved height distribution of (c) and (d), respectively.

board is around 35 μm. Figures 10(c) and 10(d) are the fringe images of the measured areas. The retrieved 3D models are presented in Figs. 10(e) and 10(f), respectively, from which we can clearly observe that the metal pins and the solder-resist ink are separated except for the areas connecting the pins and the microstrip lines. The microstrip lines in Fig. 10(e) are not recognized clearly because the lines are covered with the ink, and thus the height difference becomes almost inconspicuous.

Due to the synchronization of the high-speed projector and camera, the proposed dual-pattern-based MEFTP is very suited for dynamic 3D measurement. Compared with the commonly used phase-shifting method that uses at least three images to get the phase map wrapped in $[-\pi, \pi)$, MEFTP FTP only uses two images and meanwhile recovers the absolute phase map. Besides, the MEFTP method is not as sensitive to motion as the phase-shifting method. To demonstrate the advantage of MEFTP, we conducted dynamic 3D measurement of a vibrating diaphragm using both the phase-shifting method and MEFTP, respectively. Figure 11(a) shows the measured area of the diaphragm. Figure 11(b) is the vibrating curve of the diaphragm that was detected by MEFTP. The density of the projected fringe pattern for both methods is the same to guarantee a fair comparison.

On the vibrating curve, a green and a red point are labeled to represent two moments. The green point means the diaphragm is at its lowest position, thus the instant speed is the slowest. The red point means the diaphragm is moving towards its highest position, thus the instant speed is the fastest. The reconstructed 3D models of the vibrating diaphragm at the two

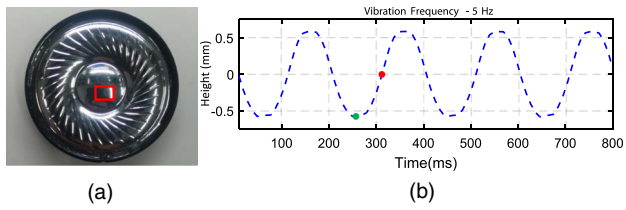


**Fig. 11.** Information of the vibrating diaphragm. (a) The measured area of the diaphragm; (b) the vibrating curve of the diaphragm.

moments are presented in Fig. 12. Figures 12(a) and 12(b) are the 3D models in the red point using the phase-shifting algorithm and MEFTP, respectively. When the diaphragm passes through the red position, the ripples as shown in Fig. 12(a) are severe because the phase-shifting algorithm is very sensitive to motion, while the result using MEFTP as shown in Fig. 12(b) is much better. Figures 12(c) and 12(d) are the 3D models in the green point using the phase-shifting algorithm and MEFTP, respectively. When the diaphragm moves slower at the green point, the ripples as shown in Fig. 12(c) are significantly decreased because the phase-shifting algorithm performs well when measuring static scenes but is

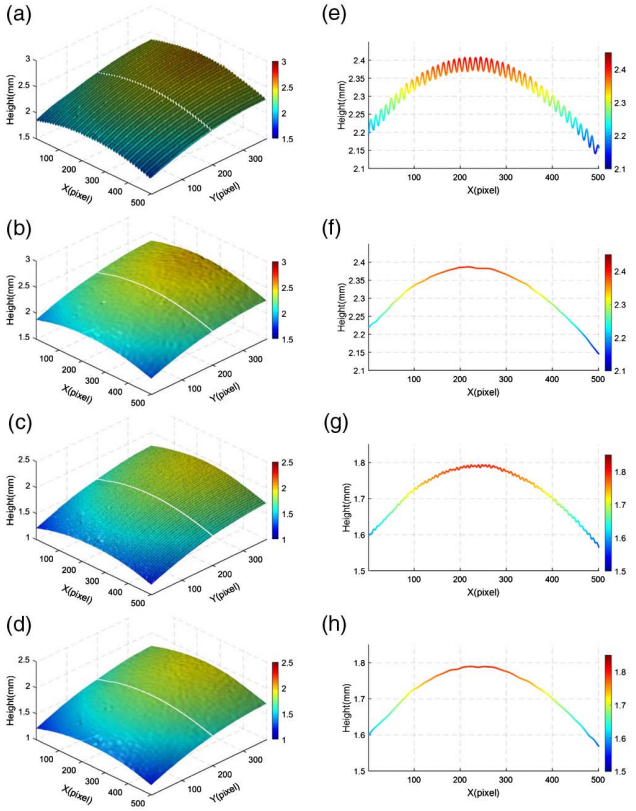


**Fig. 12.** Reconstructed 3D results of the vibrating diaphragm. (a) and (b) are 3D models corresponding to the red moment using the phase-shifting method and our proposed method, respectively; (c) and (d) are the 3D models in the green moment using the phase-shifting method and our proposed method, respectively; (e)–(h) are the cross sections corresponding to each 3D model in the left column. See Visualization 1 for more details.

still worse than the result in Fig. 12(d) using MEFTP because the diaphragm is still moving even though the speed is relatively slow. To help observe the details of the reconstructed surface, the cross section of each 3D result is given in the right column as shown in Figs. 12(e)–12(h). More details in Fig. 12 about the 3D results over time can be found in the relevant video [Visualization 1].

## 6. DISCUSSION

In the MEFTP technique, every two captured images as shown in Figs. 5(a)–5(b) generate one 3D result so that the temporal resolution depends on the time used to record two successive images. The frame speed of the projector and camera in our system is 400 frames per second, and thus 3D measurement of dynamic scenes can be realized at the speed of 200 frames per second. Although it is faster by using conventional FTP, in which only one fringe image is involved, our proposed MEFTP can provide an absolutely unwrapped phase map with higher fringe quality. Compared with the $\pi$-shift FTP, our method is not so sensitive to motion because the phase information is encoded within only one image. It should be noted that the camera and projector used in our system are both low cost, which means the performance of the technique still can be improved by using a faster digital camera and projectors.

The spatial resolution of the 3D results can be divided into lateral resolution and vertical resolution. The lateral resolution depends on the pixel pitch of the camera sensor and the whole optical magnification of the lenses. The pixel size of the used camera is 4.8 μm, and the optical magnification is around 0.5×. Thus, the lateral spatial resolution is 9.6 μm. The measurement uncertainty only comes in the depth resolution. In MEFTP, by extending the modified FTP with embedded markers, we can make the spectrum separation much easier; thus, the resolution mainly depends on the fringe density. Unlike the fringe images recorded from interferometry, the fringe image obtained from FPP has a relatively lower carrier frequency. To alleviate the side effect of the random noise, we can enlarge the whole calibrated phase range by using denser fringe. However, the fringe cannot be as dense as we want because the patterns are loaded on the DMD chip with the pixels in discrete status. Besides, too dense fringe would easily get blurred even with slight defocus. Therefore, the choice of fringe density should also be carefully treated.

Dynamic application, which is of great importance when analyzing the behavior of micro-scale products, is the most important advance of our proposed technique. In most cases, our system can provide a volume of 6 mm × 4 mm in lateral and 4 mm in depth for 3D measurement of the dynamic scenes. However, the technique still has its limitations. For some samples with steep structure, the fringe could be deformed heavily; thus, the ±1 primary spectrums could get mixed and then cannot be totally divided for further processing. Also, in order to assure effective marker detection when applying the MEFTP technique, one should make both markers located in a simply connected region as far as possible because the spatial phase unwrapping would fail to get a continuous phase map where a field of view contains discontinuous or isolated objects.

## 7. CONCLUSION

In this work, we proposed a MEFTP method by embedding two specially designed markers into a fringe pattern and a flat pattern to realize dynamic profilometry of micro-surfaces. As the basic instrument of the system, the stereomicroscope has an adjustable field of view, thus the projected fringe pattern can converge into a suited field to match the target size. In this way, we can obtain images with very dense fringe, which is better for phase retrieval using 2D Fourier transform because the wanted primary spectrum part can be more easily separated from the spectrum domain.

To avoid unsuccessful 3D reconstruction caused by the wrong detection of the marker, we propose a two-marker scheme by embedding two specially designed markers with opposite intensity distributions in the flat pattern, which provides a double proofed relative fringe order for the absolute phase map compensation. Besides, the temporal phase difference information is also introduced by comparing the average phase value between two neighboring frames, which is based the synchronization of the high-speed projector and camera. The experimental results reveal that our method effectively alleviates the spectrum aliasing effect caused by the background term. Compared with phase-shifting FPP, our system can successfully realize microscopic 3D dynamic measurement with much fewer motion-caused errors.

The projection speed reaches 400 frames per second, which greatly facilitates the dynamic 3D measurement. Only two patterns are needed to acquire the absolute phase map; thus the measurement errors caused by the motion can be effectively decreased. The proposed technique provides a solution for those who need to observe or inspect fast surface changes over time. Also, this technique also can be applied in industrial application, such as real-time quality control and online inspection, etc.

**Funding.** Final Assembly "13th Five-Year Plan" Advanced Research Project of China (30102070102); "Six Talent Peaks" project of Jiangsu Province, China (2015-DZXX-009); Fundamental Research Funds for the Central Universities (30916011322, 30917011204); National Key R&D Program of China (2017YFF0106403); National Natural Science Foundation of China (NSFC) (111574152, 61705105, 61722506); Outstanding Youth Foundation of Jiangsu Province of China (BK20170034); National Defense Science and Technology Foundation of China (0106173); "333 Engineering" Research Project of Jiangsu Province, China (BRA2016407); Open Research Fund of Jiangsu Key Laboratory of Spectral Imaging & Intelligent Sense (3091601410414); China Postdoctoral Science Foundation (2017M621747); Jiangsu Planned Projects for Postdoctoral Research Funds (1701038A).

## REFERENCES

1. S. S. Gorthi and P. Rastogi, "Fringe projection techniques: whither we are?" Opt. Lasers Eng. **48**, 133–140 (2010).
2. Q. Zhang and X. Su, "High-speed optical measurement for the drumhead vibration," Opt. Express **13**, 3110–3116 (2005).

3. S. Zhang, "Recent progresses on real-time 3D shape measurement using digital fringe projection techniques," Opt. Lasers Eng. **48**, 149–158 (2010).
4. C. Zuo, Q. Chen, G. Gu, S. Feng, and F. Feng, "High-speed three-dimensional profilometry for multiple objects with complex shapes," Opt. Express **20**, 19493–19510 (2012).
5. H. Zhao, X. Liang, X. Diao, and H. Jiang, "Rapid in-situ 3D measurement of shiny object based on fast and high dynamic range digital fringe projector," Opt. Lasers Eng. **54**, 170–174 (2014).
6. S. Feng, Q. Chen, C. Zuo, J. Sun, and S. L. Yu, "High-speed real-time 3-D coordinates measurement based on fringe projection profilometry considering camera lens distortion," Opt. Commun. **329**, 44–56 (2014).
7. Y. Hu, Q. Chen, T. Tao, H. Li, and C. Zuo, "Absolute three-dimensional micro surface profile measurement based on a greenough-type stereomicroscope," Meas. Sci. Technol. **28**, 045004 (2017).
8. G. Sansoni, M. Carocci, and R. Rodella, "Three-dimensional vision based on a combination of gray-code and phase-shift light projection: analysis and compensation of the systematic errors," Appl. Opt. **38**, 6565–6573 (1999).
9. C. Zuo, L. Huang, M. Zhang, Q. Chen, and A. Asundi, "Temporal phase unwrapping algorithms for fringe projection profilometry: a comparative review," Opt. Lasers Eng. **85**, 84–103 (2016).
10. S. Lei and S. Zhang, "Flexible 3-D shape measurement using projector defocusing," Opt. Lett. **34**, 3080–3082 (2009).
11. C. Zuo, Q. Chen, G. Gu, S. Feng, F. Feng, R. Li, and G. Shen, "High-speed three-dimensional shape measurement for dynamic scenes using bi-frequency tripolar pulse-width-modulation fringe projection," Opt. Lasers Eng. **51**, 953–960 (2013).
12. C. Zuo, T. Tao, S. Feng, L. Huang, A. Asundi, and Q. Chen, "Micro Fourier transform profilometry (μFTP): 3D shape measurement at 10,000 frames per second," Opt. Lasers Eng. **102**, 70–91 (2018).
13. X. Su and W. Chen, "Fourier transform profilometry: a review," Opt. Lasers Eng. **35**, 263–284 (2001).
14. Z. Zhang, D. P. Towers, and C. E. Towers, "Snapshot color fringe projection for absolute three-dimensional metrology of video sequences," Appl. Opt. **49**, 5947–5953 (2010).
15. M. A. Herráez, D. R. Burton, M. J. Lalor, and M. A. Gdeisat, "Fast two-dimensional phase-unwrapping algorithm based on sorting by reliability following a noncontinuous path," Appl. Opt. **41**, 7437–7444 (2002).
16. X. Su and W. Chen, "Reliability-guided phase unwrapping algorithm: a review," Opt. Lasers Eng. **42**, 245–261 (2004).
17. Q. Kemao, W. Gao, and H. Wang, "Windowed Fourier-filtered and quality-guided phase-unwrapping algorithm," Appl. Opt. **47**, 5420–5428 (2008).
18. H. Guo and P. Huang, "3D shape measurement by use of a modified Fourier transform method," Proc. SPIE **7066**, 70660E (2008).
19. S. Zhang and P. S. Huang, "Novel method for structured light system calibration," Opt. Eng. **45**, 083601 (2006).
20. M. Takeda, H. Ina, and S. Kobayashi, "Fourier-transform method of fringe-pattern analysis for computer-based topography and interferometry," J. Opt. Soc. Am. **72**, 156–160 (1982).
21. X.-Y. Su, J. Li, L.-R. Guo, and W.-Y. Su, "An improved Fourier transform profilometry," Proc. SPIE **0954**, 241–245 (1989).
22. E. Hu and Y. He, "Surface profile measurement of moving objects by using an improved π phase-shifting Fourier transform profilometry," Opt. Lasers Eng. **47**, 57–61 (2009).
23. Q. Kemao, "Windowed Fourier transform for fringe pattern analysis," Appl. Opt. **43**, 2695–2702 (2004).
24. S. Zhang and S.-T. Yau, "High-resolution, real-time 3D absolute coordinate measurement based on a phase-shifting method," Opt. Express **14**, 2644–2649 (2006).
25. S. Zhang, D. Royer, and S.-T. Yau, "GPU-assisted high-resolution, real-time 3-D shape measurement," Opt. Express **14**, 9120–9129 (2006).
26. H. Cui, W. Liao, N. Dai, and X. Cheng, "A flexible phase-shifting method with absolute phase marker retrieval," Measurement **45**, 101–108 (2012).
27. Z. Zhang, "A flexible new technique for camera calibration," IEEE Trans. Pattern Anal. Mach. Intell. **22**, 1330–1334 (2000).
28. Y. Hu, Q. Chen, S. Feng, T. Tao, H. Li, and C. Zuo, "Real-time microscopic 3-D shape measurement based on optimized pulse-width-modulation binary fringe projection," Meas. Sci. Technol. **28**, 075010 (2017).